Gradient-Modulated PETRA MRI

Naoharu Kobayashi, Ute Goerke, Luning Wang, Jutta Ellermann, Gregory J. Metzger, and Michael Garwood

Center for Magnetic Resonance Research, Department of Radiology, University of Minnesota, Minneapolis, MN

Corresponding Author:
Naoharu Kobayashi, PhD
Center for Magnetic Resonance Research, Department of Radiology,
University of Minnesota, 2021 Sixth Street SE, Minneapolis, MN
55455; E-mail: naoharu@cmrr.umn.edu

Key Words: magnetic resonance imaging, ultrashort echo time, pointwise-encoding time reduction with radial acquisition, image blurring, off-resonance

Abbreviations: Echo time (TE), field of view (FOV), flip angle (FA), gradient echo (GRE), gradient modulation (GM), magnetic resonance imaging (MRI), maximum intensity projection (MIP), pointwise-encoding time reduction with radial acquisition (PETRA), radiofrequency (RF), retention time (TR), single-point imaging (SPI), specific absorption rate (SAR), transmit and receive (T/R), zero echo time (ZTE), pulse width (pw)

ABSTRACT

Image blurring that results from off-resonance and fast T_2* signal decay is a common issue in radial ultrashort echo time magnetic resonance imaging (MRI) sequences. One solution is to use a higher readout bandwidth, but this may be impractical for some techniques such as pointwise-encoding time reduction with radial acquisition (PETRA), which is a hybrid method of zero echo time and single-point imaging techniques. Specifically, PETRA has severe specific absorption rate (SAR) and radiofrequency (RF) pulse peak power limitations when using higher bandwidths in human measurements. In this study, we introduce gradient modulation (GM) to PETRA to reduce image-blurring artifacts while keeping SAR and RF peak power low. GM-PETRA tolerance to image blurring was evaluated in simulations and experiments by comparison with the conventional PETRA technique. We performed inner ear imaging of a healthy subject at 7 T. GM-PETRA showed significantly less image blurring as a result of off-resonance and fast T_2* signal decay compared to PETRA. In in vivo imaging, GM-PETRA nicely captured complex structures of the inner ear such as the cochlea and semicircular canals. GM can improve PETRA image quality and mitigate SAR and RF peak power limitations without special hardware modification in clinical scanners.

INTRODUCTION

Image blurring that results from off-resonance and fast signal decay of extremely short T_2* spins is a common problem for radial ultrashort echo time magnetic resonance imaging (MRI) sequences such as zero echo time (ZTE) (1, 2) and sweep imaging with Fourier transformation (3) techniques. Although higher static magnetic field strengths have a signal-to-noise ratio advantage, such image blurring is even more severe because of increasing chemical shifts and accelerated T_2* signal decay. One efficient and simple solution for this image-blurring issue is to use a higher readout bandwidth.

In the ZTE technique, gradients are turned on before applying the radiofrequency (RF) excitation pulse (a constant-amplitude "hard" pulse), and the gradient amplitude remains constant during the ensuing data acquisition. Therefore, excitation and readout bandwidths need to be the same; a higher readout bandwidth results in a higher excitation bandwidth. However, a high excitation bandwidth (ie, short pulse length) leads to an increase in the specific absorption rate (SAR) and RF pulse peak power, which are the major limitations of ZTE in human applications (4). Another severe limitation of using higher bandwidths in ZTE is an increasing demand for fast switching between transmit and receive (T/R) modes. The slow T/R switching of most standard clinical MRI scanners ($>$20 μs) results in missing critical data points in a large region around the center of k-space (5).

Pointwise-encoding time reduction with radial acquisition (PETRA) has been recently introduced (6, 7) and overcomes the T/R switching limitation of clinical scanners by combining ZTE and single-point imaging (SPI) (8). PETRA acquires the missing k-space center region in ZTE with additional SPI acquisitions. However, although PETRA alleviates the requirement on fast T/R switching, the use of a higher bandwidth increases the number of missing k-space center points. Accordingly, higher bandwidths along with slow T/R switching in clinical scanners results in a large missing region around the k-space center, namely a long additional SPI acquisition time.

We introduce herein a novel PETRA technique with gradient modulation (GM) that enables high readout bandwidths while keeping a relatively low excitation bandwidth. GM significantly reduces SAR and RF peak power and keeps the missing center k-space region small. Tolerance to image blurring as a result of off-resonance and fast T_2* signal decay was evaluated in simulation and experimentally by comparing PETRA with and without GM. Finally, we conducted inner ear imaging of a normal subject at 7 T.

METHODOLOGY

GM-PETRA

In PETRA, signal acquisition starts immediately after a hard pulse excitation and the following T/R switching delay (t_s) using gradi-

ISSN 2379-1381 http://dx.doi.org/10.18383/j.tom.2015.00157

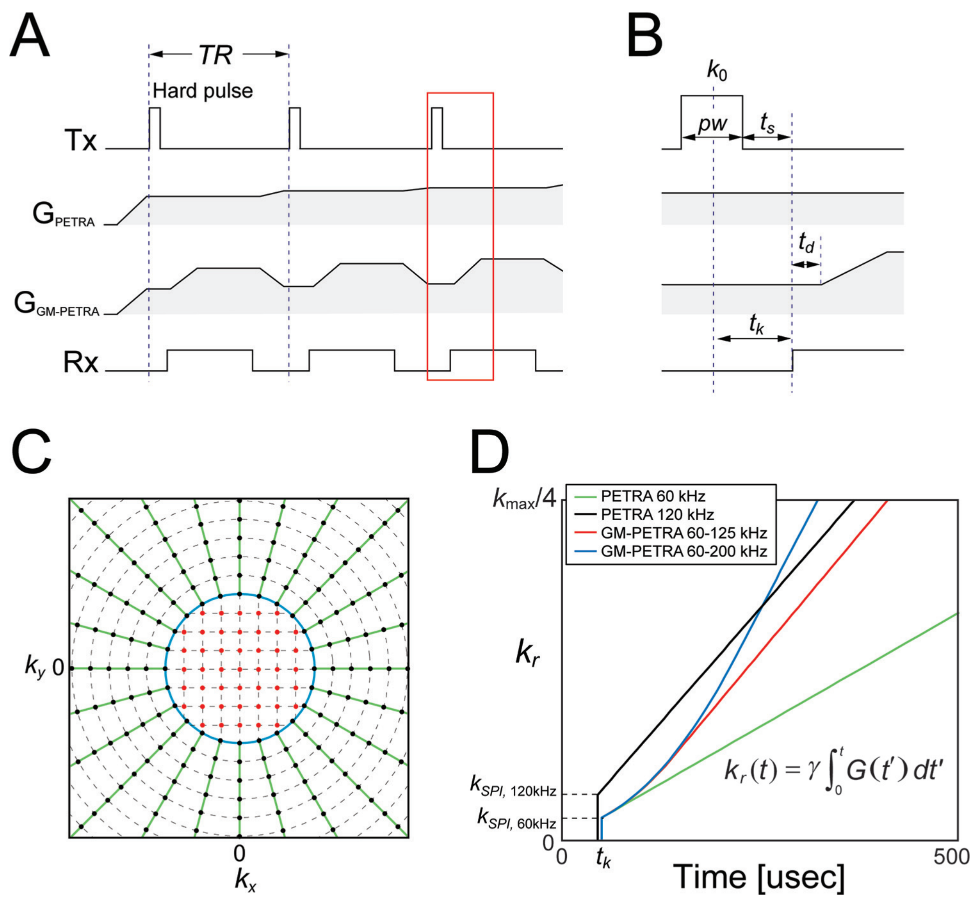

Figure 1. (A) Sequence diagram of PETRA with and without GM and magnification of the region around excitation shown by a red box (B). GM-PETRA is identical to PETRA until gradients start ramping up. (C) *k*-space sampling in PETRA and GM-PETRA is a hybrid of 2 sampling strategies. The center region is sampled with SPI (red points) and the peripheral region by radial readout (green lines). The boundary of the 2 sampling regions (k_{SPI}) is limited by $t_k = pw/2 + t_s$ ($k_{\mathrm{SPI}} = \gamma G_{ex} \cdot t_k$; blue circle). (D) GM-PETRA samples *k*-space more quickly by increasing the gradient amplitude after excitation. Although PETRA sampling with a high bandwidth (120 kHz) achieves faster sampling around the *k*-space center, GM-PETRA with lower excitation bandwidth (G_{ex} = 60 kHz) catches up on it quickly as the gradient modulation increases (G_{max}= 125 and 200 kHz).

ents with constant amplitude (G_{ex}) (Figure 1A) with radial *k*-space sampling (6). Because the *k*-space center is located at the center of the hard pulse, *k*-space center points are not sampled during the first $t_k = pw/2 + t_s$ period, where pw is pulse width of the hard pulse, as shown in Figure 1B. Therefore, t_k limits available echo time (TE). The missing *k*-space center points are acquired using SPI (8) and satisfy $|\mathbf{k}| < \gamma G_{ex} \cdot t_k = k_{\mathrm{SPI}}$, where γ is the gyromagnetic ratio. In SPI, *k*-space samples are acquired 1 by 1, thus stepwise reducing the gradient amplitude. Accordingly, *k*-space sampling in PETRA is a hybrid of 2 sampling strategies: radial and SPI (Figure 1C).

In GM-PETRA, after the receiver gate is turned on, the gradient amplitude starts ramping up from G_{ex} to G_{max}, followed by an inserted short delay time (t_d); the delay time with flat gradients is used for acquiring missing *k*-space points in the SPI acquisition (Figure 1A, B). Under the same excitation bandwidth conditions, PETRA and GM-PETRA are identical until the gradients start ramping up. By increasing the gradient amplitude (readout bandwidth), *k*-space is sampled more quickly (Figure 1D). Moreover, having a lower bandwidth in excitation than readout in GM-PETRA reduces the amount of RF peak power and SAR. For conventional pulses such as the hard pulse, RF peak power, B_{1max}, and SAR have the following relations with respect to flip angle (FA), α, and the excitation bandwidth (BW_{ex}):

$$B_{1max} \propto \alpha \cdot BW_{ex} \tag{1}$$

$$\mathrm{SAR} \propto \alpha^2 \cdot BW_{ex} \tag{2}$$

Therefore, a lower BW_{ex} reduces SAR and RF peak power. Another advantage of using a lower excitation bandwidth is the reduction of missing points around the *k*-space center because the number of missing points in each ZTE acquisition is given by $t_k \cdot BW_{ex}$.

Simulation

To evaluate the ability of GM-PETRA to address image blurring as a result of off-resonance and short T_2^* signals, numerical simulations were conducted for a 3D Shepp–Logan phantom. The phantom contained 4 compartments: off-resonance ($\Delta\omega$ = 1050 Hz; 3.5 ppm at 7 T), on-resonance, and 2 short T_2^* values (500 and 200 μs). T_2^* values for on- and off-resonance spins were set to 40 ms, and the frequency of the short T_2^* spins was on-resonance ($\Delta\omega$ = 0 Hz). The *k*-space signal $S(\mathbf{k})$ was calculated by

$$S(\mathbf{k}) = s(\mathbf{k}) \cdot e^{2\pi i \cdot \Delta\omega t} \cdot e^{-t/T_2^*} \tag{3}$$

$$\mathbf{k}(t) = \int_0^t \gamma \mathbf{G}(t')\mathrm{d}t' \tag{4}$$

where $s(\mathbf{k})$ is the *k*-space without off-resonance and T_2^* signal decay, $\mathbf{G}(t)$ is a gradient vector in 3D space, t is the sampling time after the center of the hard pulse excitation (*k*-space center), and $\mathbf{k}(t)$ is the 3D *k*-space coordinates. A plot of

$k_r(t) = |k(t)|$ is shown in Figure 1D. Simulations were performed with excitation bandwidths of 60 and 120 kHz in PETRA and a 60-kHz excitation followed by bandwidth increases to 125 and 200 kHz in GM-PETRA.

Experiments

All experiments were performed with a 7 T MRI scanner (Siemens, Erlangen, Germany) using a head coil with 8 transceiver and 24 receiver channels (Nova Medical, Wilmington, MA). For B_1^+ shimming, complex B_1^+ maps were estimated for each of the 8 transmit channels using a fast, low-FA, multichannel B_1^+ calibration scan (9). A B_1^+ shim solution was optimized to maximize the efficiency over a selected region of interest (10).

To test image blurring caused by off-resonance and/or short T_2^* signals, a breast phantom and apple were imaged with PETRA and GM-PETRA. The breast phantom had fat and water compartments inside ($\Delta\omega$ = 1050 and 0 Hz, respectively). The excitation bandwidth (γG_{ex} · field of view [FOV]) was set to 60 kHz, which provided pw of 20 μs and TE of 50 μs. The following parameters were used in PETRA and GM-PETRA: FA = 5°; retention time (TR) = 5 ms; total acquisitions = 65 536, including 123 SPI acquisitions; and scan time = 5 min 29 s. For PETRA, a higher excitation bandwidth of 120 kHz was also tested for comparison, where TE = 45 μs and 925 SPI acquisitions were needed. In GM-PETRA, the gradient modulation was set to γG_{max} · FOV = 125 and 200 kHz as in the simulations. The slew rate of the ramping gradient was fixed to 100 mT/m/ms (50% of the maximum slew rate) to avoid deleterious effects from eddy currents, resulting in a ramping time of 60-80 and 120-170 μs for 125 and 200 kHz, respectively. For imaging the apple, a conventional 3D gradient echo (GRE) acquisition was performed to demonstrate its short T_2^* signal decay, which resulted from the large volume of intercellular air spaces (11); the TE was set to its minimum of 2.8 ms. The other parameters were TR = 5.8 ms and scan time = 5 min 23 s.

Inner ear imaging of a healthy subject was conducted under an approved internal review board protocol. Sequence parameters were set to the same as those in the breast phantom and apple imaging, but FA was 4° because of a severe SAR limitation at 7 T. PETRA acquisition was carried out only with a 60-kHz excitation because 120 kHz exceeded the SAR limit. 3D GRE imaging was also performed for comparison.

Image reconstruction was performed offline with a home-built program written in C++/CUDA (NVIDIA, Santa Clara, CA). K-space sampling density, including the effects from the ramp sampling in GM-PETRA, was compensated by the iterative density correction (12). The density-corrected radial k-space data were reconstructed to a 3D image with nonuniform fast Fourier transform (13).

RESULTS

Simulation

Simulations showed that off-resonance blurring ("duplicated edges" around the off-resonance compartment) improved as the bandwidth increased (Figure 2); blurry edges got thinner for higher bandwidths. By increasing the GM-PETRA amplitude from 60 to 125 kHz (GM-PETRA 60-125 kHz), off-resonance artifacts became comparable to PETRA with a 120-kHz excitation (PETRA

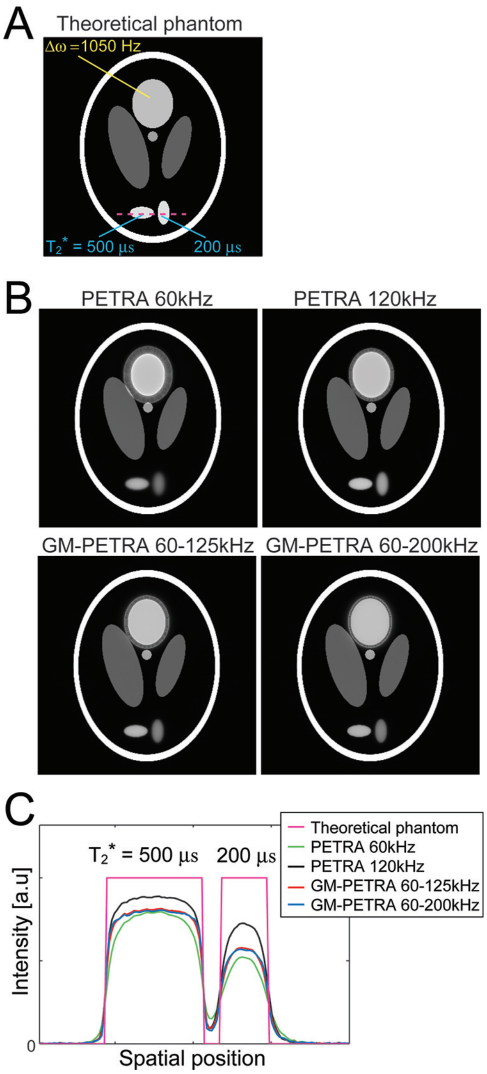

Figure 2. Numerical simulation of image-blurring artifacts resulting from off-resonance and fast T_2^* decay. (A) Simulations performed for a Shepp–Logan phantom with off-resonance ($\Delta\omega$ = 1050 Hz; 3.5 ppm at 7 T) and short T_2^* spins (T_2^* = 200 and 500 μs). (B) Image blurring ("duplicated edges" around the off-resonance spins) leads to thinner PETRA and GM-PETRA as a result of increasing bandwidth. Although the excitation bandwidth is lower in GM-PETRA, the thickness of the duplicated edge was comparable to PETRA 120 kHz for GM-PETRA 60–125 kHz and thinner for GM-PETRA 60–200 kHz. (D) For short T_2^* image blurring, edge sharpness was improved along with an increase of the bandwidth, which is clearer on the intensity plots along the line through the short T_2^* compartments (dashed line in A).

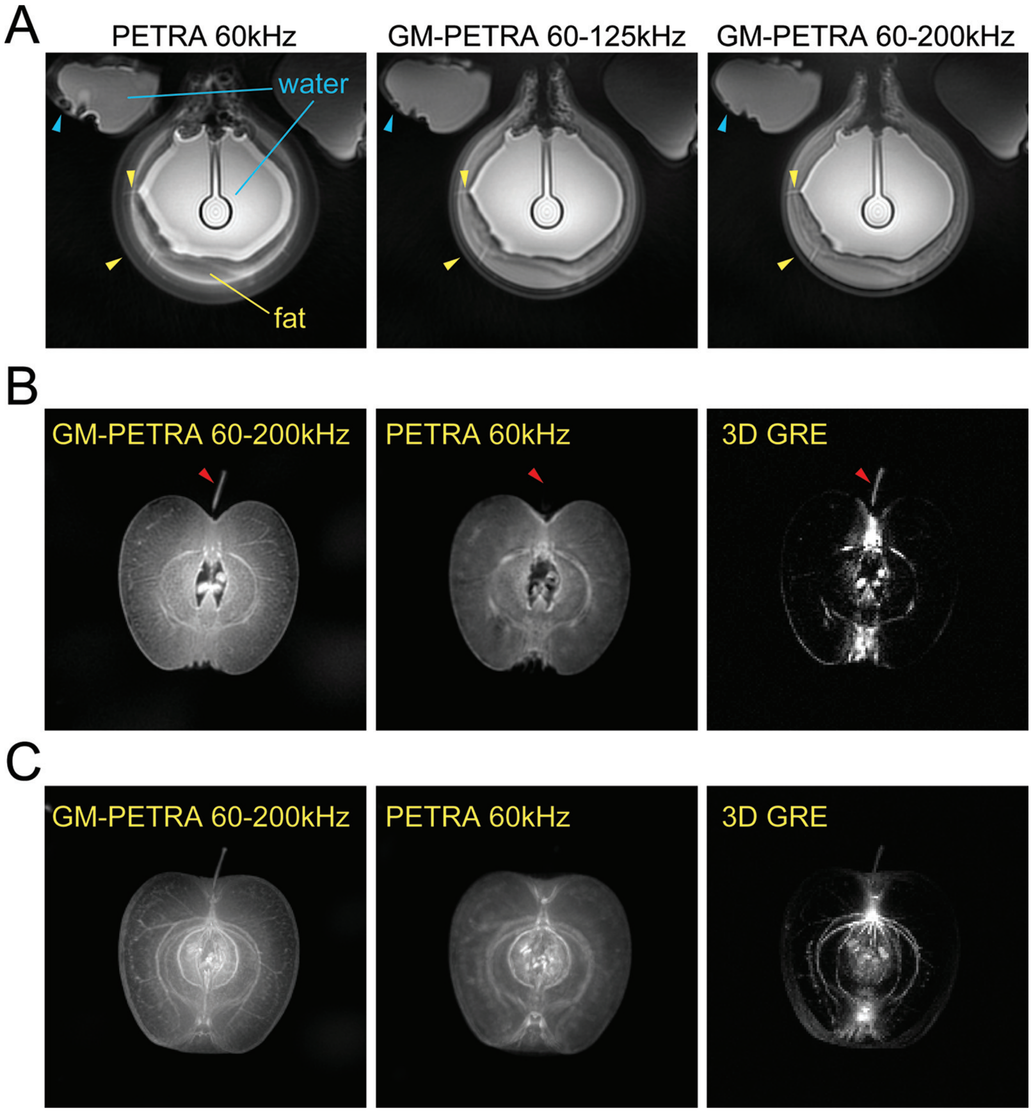

Figure 3. (A) Improvement of the off-resonance artifacts as a result of chemical shift (fat-water) and susceptibility differences in a phantom experiment with GM-PETRA. Duplicated edges around fat regions became thinner as the GM increased; small gaps between fat compartments were visualized better in images from higher bandwidth (yellow arrowheads). Image blurring and distortion around the edges of water compartments also improved along with an increase of the bandwidth (light blue arrowheads). PETRA 120 kHz showed similar image blurring artifacts to GM-PETRA 60–125 kHz (data not shown), which is consistent with the simulation results shown in Figure 2. (B) Image blurring as a result of short T_2* decay and/or off-resonance demonstrated in an apple imaging. GM-PETRA allowed finer structures in the mesocarp (flesh) to be appreciated compared to PETRA; these structures were completely invisible in 3D GRE because of their very short T_2* values. Although the calyx had a relatively long T_2* (which makes it visible with 3D GRE), it was completely blurred out with PETRA because of strong susceptibility effects (red arrowheads). (C) An MIP image from GM-PETRA clearly allows fine structures in the mesocarp to be appreciated, including fibers compared to the other 2 acquisition methods.

120 kHz). GM-PETRA 60-200 kHz showed further improvement as a result of reduced off-resonance blurring. For short T_2* spins, increasing the bandwidth improved edge sharpness (Figure 1C). PETRA 120 kHz showed an increased ability to preserve short T_2* signals (ie, higher signal intensities), especially for spins with $T_2^* = 200\ \mu s$, because of its shorter TE and faster sampling around the *k*-space center (Figure 1D). To preserve extremely short T_2* signals, higher excitation bandwidths are desirable.

Experiments

Breast phantom images with PETRA and GM-PETRA were consistent with simulation results (Figure 3A); the off-resonance blurring that resulted from the chemical shift of fat and magnetic susceptibility differences were improved as the bandwidth increased. In apple imaging, GM-PETRA and PETRA showed higher sensitivity to signals from the mesocarp (flesh) that was almost invisible with 3D GRE because of its extremely fast T_2*

Figure 4. (A) In vivo imaging of a healthy volunteer's inner ear. Complex structures in the inner ear were well visualized with GM-PETRA compared to PETRA and 3D GRE. PETRA had a high sensitivity to short T_2* signals that was comparable to GM-PETRA but suffered from severe image blurring (ie, missing structures) because of strong susceptibility differences at the air-tissue interfaces (light blue arrowheads). The strong susceptibility differences accelerated the T_2* signal decay, making it difficult to visualize some structures of the inner ear (eg, small nerves) with 3D GRE (yellow arrowheads). (B) MIP images calculated for GM-PETRA by masking out the surrounding tissues around the inner ear. The MIP images allowed complex structures in the inner ear to be visualized. MIP images projected to different image planes are available in the online Supplemental Materials (PLAY VIDEO).

signal decay (Figure 3B). The PETRA image was visually blurry compared to GM-PETRA because of off-resonance associated with susceptibility differences and fast T_2* signal decay. In maximum intensity projection (MIP) images, GM-PETRA visualized fine structures in the apple better than the other 2 methods (Figure 3C). 3D GRE also visualized structures such as vascular bundles, endocarp (core), and exocarp (skin), but many of fine structures in the mesocarp were missing.

Visualization of small structures in the inner ear was improved by GM-PETRA (Figure 4A). Although PETRA and GM-PETRA had comparable sensitivity to short T_2* signals, PETRA suffered from severe image blurring mainly because of strong susceptibility differences at the air-tissue interfaces. The strong susceptibility differences also accelerated T_2* signal decay and made it difficult to visualize some structures in the inner ear (eg, small nerves) with 3D GRE. MIP images of the GM-PETRA data allowed complex structures of the inner ear such as cochlea and semicircular canals to be nicely visualized (Figure 4B).

DISCUSSION

Gradient modulation has been introduced in the PETRA technique to increase readout bandwidth, which, in turn, can reduce image-blurring artifacts resulting from off-resonance and T_2* signal decay. This work demonstrates how gradient modulation enables flexible settings of excitation and readout bandwidths. The possibility of using a decreased excitation bandwidth while keeping the readout bandwidth high can alleviate the severe limitations in clinical applications imposed by SAR and RF peak power, which are proportional to excitation bandwidth (Equations 1 and 2).

Gradient modulation was previously implemented to increase achievable flip angles and to reduce off-resonance blurring in radial ultrashort TE techniques (14-16). One benefit of the higher flip-angle availability in GM-PETRA is to achieve stronger T_1-weighted image contrasts, whereas many ultrashort TE techniques provide mostly proton density-weighted contrasts because of their relatively low flip angles. In ZTE, as the bandwidth increases, achievable flip angles were severely limited as a result of short pulse widths. When a longer pulse is used, the sinc-shaped excitation profile of the hard pulse causes blurring artifacts around the edges of the FOV. This issue was addressed in previous studies by correcting the sinc-shaped profile in image reconstruction (17) or by using frequency- (or phase-) modulated pulses to flatten the excitation profile (18, 19). By combining gradient modulation with frequency-modulated pulse excitation, the limitation can be further alleviated. However, because frequency-modulated pulse excitation generates a nonlinear phase distribution in space (20), one needs to handle the nonlinear phase by using methods such as algebraic (18, 21) and iterative (19) reconstruction methods.

One disadvantage of using gradient modulation is an increase of acoustic noise, as compared with the original PETRA sequence, which is extremely quiet (6, 7). Therefore, there is a tradeoff between GM-PETRA's increased acoustic noise and its ability to decrease blurring artifacts and mitigated SAR and/or RF peak power limitations. Moreover, as the bandwidth increases, the sequence becomes more sensitive to gradient performance, including group delays and eddy currents. Gradient miscalibration may thereby induce image quality degradation.

Another tradeoff of using higher bandwidths in GM-PETRA while keeping other sequence parameters fixed (as in this study) is between reduced image blurring and SNR. Although a conspicuous increase of noise was not observed with the current settings of up to 200 kHz at 7 T, randomly distributed noise can be efficiently removed by applying image reconstructions with regularization such as with compressed sensing (22-24). Such image reconstruction methods can improve image quality as well as accelerate data acquisition by extracting information from coil sensitivity variations between multiple receiver coils and sparsity in an appropriate transform domain (eg, wavelet and total variation).

In conclusion, GM-PETRA showed significantly less image blurring as a result of off-resonance and fast T_2^* signal decay compared to the conventional PETRA technique. Gradient modulation can improve PETRA image quality and mitigate the limitation on SAR and RF peak power without requiring specific hardware modifications on clinical scanners.

Supplemental Materials:
Video: http://tiny.cc/tom-01-02-s003

ACKNOWLEDGMENTS

This study was supported by National Institutes of Health grants P41EB015894 and S10RR026783 and the W.M. Keck Foundation.

REFERENCES

1. Hafner S. Fast imaging in liquids and solids with the Back-projection Low Angle ShoT (BLAST) technique. Magn Reson Imaging. 1994;12(7):1047–1051.
2. Weiger M, Pruessmann KP, Hennel F. MRI with zero echo time: hard versus sweep pulse excitation. Magn Reson Med. 2011;66(2):379–389.
3. Idiyatullin D, Corum C, Park JY, Garwood M. Fast and quiet MRI using a swept radiofrequency. J Magn Reson. 2006;181(2):342–349.
4. Weiger M, Brunner DO, Dietrich BE, Muller CF, Pruessmann KP. ZTE imaging in humans. Magn Reson Med. 2013;70(2):328–332.
5. Kuethe DO, Caprihan A, Lowe IJ, Madio DP, Gach HM. Transforming NMR data despite missing points. J Magn Reson. 1999;139(1):18–25.
6. Grodzki DM, Jakob PM, Heismann B. Ultrashort echo time imaging using pointwise encoding time reduction with radial acquisition (PETRA). Magn Reson Med. 2012;67(2):510–518.
7. Ida M, Wakayama T, Nielsen ML, Abe T, Grodzki DM. Quiet T1-weighted imaging using PETRA: initial clinical evaluation in intracranial tumor patients. J Magn Reson Imag. 2015;41(2):447–453.
8. Balcom BJ, Macgregor RP, Beyea SD, Green DP, Armstrong RL, Bremner TW. Single-Point Ramped Imaging with T1 Enhancement (SPRITE). J Magn Reson Ser A. 1996;123(1):131–134.
9. Van de Moortele PF, Ugurbil K. Very fast multi channel B1 calibration at high field in the small flip angle regime. Proc Int Soc Magn Reson Med. 2009;17:367.
10. Metzger GJ, Snyder C, Akgun C, Vaughan T, Ugurbil K, Van de Moortele PF. Local B1+ shimming for prostate imaging with transceiver arrays at 7T based on subject-dependent transmit phase measurements. Magn Reson Med. 2008;59(2):396–409.
11. Musse M, De Guio F, Quellec S, Cambert M, Challois S, Davenel A. Quantification of microporosity in fruit by MRI at various magnetic fields: comparison with X-ray microtomography. Magn Reson Imaging. 2010;28(10):1525–1534.
12. Pipe JG, Menon P. Sampling density compensation in MRI: rationale and an iterative numerical solution. Magn Reson Med. 1999;41(1):179–186.
13. Fessler JA, Sutton BP. Nonuniform fast Fourier transforms using min-max interpolation. IEEE Trans Signal Processing. 2003;51(2):560–574.
14. Kobayashi N, Garwood M. B1 mapping of short T2 * spins using a 3D radial gradient echo sequence. Magn Reson Med. 2014;71(5):1689–1699.
15. Zhang J, Idiyatullin D, Corum CA, Kobayashi N, Garwood M. Gradient-modulated SWIFT. Magn Reson Med. 2015.
16. Kobayashi N, Lei J, Utecht L, Garwood M, Ingbar DH, Bhargava M. 3D cine magnetic resonance imaging of rat lung ARDS using gradient-modulated SWIFT with retrospective respiratory gating. Proc SPIE Int Soc Opt Eng. 2015;9417.
17. Grodzki DM, Jakob PM, Heismann B. Correcting slice selectivity in hard pulse sequences. J Magn Reson. 2012;214(1):61–67.
18. Schieban K, Weiger M, Hennel F, Boss A, Pruessmann KP. ZTE imaging with enhanced flip angle using modulated excitation. Magn Reson Med. 2015;74(3):684–693.
19. Li C, Magland JF, Seifert AC, Wehrli FW. Correction of excitation profile in Zero Echo Time (ZTE) imaging using quadratic phase-modulated RF pulse excitation and iterative reconstruction. IEEE Trans Med Imaging. 2014;33(4):961–969.
20. Garwood M, DelaBarre L. The return of the frequency sweep: designing adiabatic pulses for contemporary NMR. J Magn Reson. 2001;153(2):155–177.
21. Weiger M, Hennel F, Pruessmann KP. Sweep MRI with algebraic reconstruction. Magn Reson Med. 2010;64(6):1685–1695.
22. Lustig M, Donoho D, Pauly JM. Sparse MRI: the application of compressed sensing for rapid MR imaging. Magn Reson Med. 2007;58(6):1182–1195.
23. Block KT, Uecker M, Frahm J. Undersampled radial MRI with multiple coils. Iterative image reconstruction using a total variation constraint. Magn Reson Med. 2007;57(6):1086–1098.
24. Feng L, Grimm R, Block KT, Chandarana H, Kim S, Xu J, Axel L, Sodickson DK, Otazo R. Golden-angle radial sparse parallel MRI: Combination of compressed sensing, parallel imaging, and golden-angle radial sampling for fast and flexible dynamic volumetric MRI. Magn Med. 2014;72(3):707–717.